Icarus 205 (2010) 627–637

Contents lists available at ScienceDirect

Icarus

journal homepage: www.elsevier.com/locate/icarus

Energy balance of the Deep Impact experiment

O. Groussin [a,*], M. A'Hearn [b], M.J.S. Belton [c], T. Farnham [b], L. Feaga [b], J. Kissel [d], C.M. Lisse [e], J. Melosh [f], P. Schultz [g], J. Sunshine [b], J. Veverka [h]

[a] Laboratoire d'Astrophysique de Marseille, Université de Provence, CNRS, 13388 Marseille Cedex 13, France
[b] University of Maryland, College Park, MD 20740, USA
[c] Belton Space Exploration Initiatives, Tucson, AZ 85716, USA
[d] MPI, 37191 Katlenburg-Lindau, Germany
[e] Applied Physics Laboratory, Laurel, MD 20723, USA
[f] Lunar and Planetary Laboratory, Tucson, AZ 85721, USA
[g] Brown University, Providence, RI 02912, USA
[h] Cornell University, Ithaca, NY 14853, USA

ARTICLE INFO

Article history:
Received 24 April 2009
Revised 22 July 2009
Accepted 24 July 2009
Available online 28 August 2009

Keywords:
Comets
Comet Tempel-1
Comets, Composition

ABSTRACT

We present results on the energy balance of the Deep Impact experiment based on analysis of 180 infrared spectra of the ejecta obtained by the Deep Impact spacecraft. We derive an output energy of 16.5 (+9.1/−4.1) GJ. With an input energy of 19.7 GJ, the error bars are large enough so that there may or may not be a balance between the kinetic energy of the impact and that of outflowing materials. Although possible, no other source of energy other than the impactor or the Sun is needed to explain the observations. Most of the energy (85%) goes into the hot plume in the first few seconds, which only represents a very small fraction (<0.01%) of the total ejected mass. The hot plume contains 190 (+263/−71) kg of H_2O, 1.6 ± 0.5 kg of CO_2, 8.2 (+11.3/3.1) kg of CO (assuming a CO/H_2O ratio of 4.3%), 27.9 (+25.0/−8.9) kg of organic material and 255 ± 128 kg of dust, while the ejecta contains $\sim 10^7$ kg of materials. About 12% of the energy goes into the ejecta (mostly water) and 3% to destroy the impactor. Volatiles species other than H_2O (CO_2, CO or organic molecules) contribute to <7% of the energy balance. In terms of physical processes, 68% of the energy is used to accelerate grains (kinetic energy), 16% to heat them, 6% to sublimate or melt them and 10% (upper limit) to break and compress dust and/or water ice aggregates into small micron size particles. For the hot plume, we derive a dust/H_2O ratio of 1.3 (+1.9/−1.0), a CO_2/H_2O ratio of 0.008 (+0.009/−0.006), an organics/H_2O ratio of 0.15 (+0.29/−0.11) and an organics/dust ratio of 0.11 (+0.30/−0.07). This composition refers to the impact site and is different from that of the bulk nucleus, consistent with the idea of layers of different composition in the nucleus sub-surface. Our results emphasize the importance of laboratory impact experiments to understand the physical processes involved at such a large scale.

1. Introduction

The Deep Impact mission successfully impacted Comet 9P/Tempel 1 on July 4, 2005 (A'Hearn et al., 2005). Numerous papers summarizing the different *in situ* and ground-based observations and analysis have been published on this event (e.g., Icarus 191, 2007; Science 210, 2005). The energy balance of the Deep Impact experiment was only partially addressed by these papers and several questions were raised, one of the most important being: is the input kinetic energy of the impactor sufficient to explain the amount *and* velocity of the materials excavated from the comet in the ejecta? A tentative answer to this question led to several discussions in, e.g., Keller et al. (2007) or Holsapple and Housen (2007), arguing that another source of energy (vaporization of icy grains) is required to accelerate the materials in order to fit the observations.

Beyond this question, the energy balance of the Deep Impact experiment provides new insights for understanding the event and the composition of the upper layers of a comet nucleus. It also offers a unique opportunity to compare and contrast this large scale experiment not only with laboratory impact experiments at smaller scale (Schultz et al., 2007), but also with theoretical simulations (Melosh, 2006). This is important to validate (or invalidate) extrapolations usually based on physical laws, from the macroscopic scale in the laboratory to the kilometric scale of real craters on Solar System objects.

* Corresponding author. Address: Laboratoire d'Astrophysique de Marseille, Technopôle de Marseille Etoile, 38 rue Frédéric Joliot-Curie, 13338 Marseille Cedex 13, France. Fax: +33 4 91 66 18 55.
E-mail address: olivier.groussin@oamp.fr (O. Groussin).

0019-1035/$ - see front matter © 2009 Elsevier Inc. All rights reserved.
doi:10.1016/j.icarus.2009.07.048

Table 1
Fluorescence ($g_\odot$) and thermal emission ($g_{thermal}$) g-factors (s^{-1}) for H_2O, CO_2 and organic molecules, as a function of temperature. $g_\odot$ is almost constant with temperature and negligible compared to $g_{thermal}$ at high temperatures. The partition function Z is given for the discussion on opacity (see text). The g-factors values have been derived from the HITRAN database.

	H_2O (2.7 μm)	H_2O (1.4 μm)	CO_2	Organics
$g_\odot$	2.90×10^{-4}	1.78×10^{-5}	2.86×10^{-3}	2.3×10^{-3}
$g_{thermal}$ @ 200 K	1.66×10^{-10}	6.44×10^{-22}	1.94×10^{-5}	–
$g_{thermal}$ @ 700 K	3.81×10^{-2}	2.84×10^{-5}	3.37	0.3[a]
$g_{thermal}$ @ 900 K	0.207	2.02×10^{-4}	9.86	1[a]
$g_{thermal}$ @ 1100 K	0.610	1.43×10^{-3}	19.5	2.0[a]
$g_{thermal}$ @ 1300 K	1.29	5.83×10^{-3}	31.2	3.1[a]
$g_{thermal}$ @ 1400 K	1.72	1.02×10^{-2}	37.5	3.8[a]
$g_{thermal}$ @ 1500 K	2.22	1.64×10^{-2}	44.1	4.4[a]
$Z(T = 37.5\ K)$	8.6	8.6	33	284[b]

[a] The value of $g_{thermal}$ for the organic component is derived from $g_{thermal}$ for CO_2. Its value is assumed to be 10 times smaller due to a partition function $Z(T)$ that is about 10 times larger than that of CO_2.
[b] Value for CH_3OH (Crovisier, 2006), the main organic component.

However, determining the energy balance of such a large experiment is a complex issue, which requires an overview of the event and the associated dataset, an understanding of the physical processes involved, and the knowledge of several key parameters estimated *in situ* by the Deep Impact spacecraft or remotely by ground-based observers. Previous work on this topic was limited because it mainly focussed on the late ejecta detected from ground-based telescopes (Meech et al., 2005) or space mission instruments (OSIRIS on Rosetta, Keller et al., 2007) and could not take into account the materials in the hot self-luminous plume. This hot plume, excavated in the first seconds after impact (A'Hearn et al., 2005), was only detected by the Deep Impact instruments and plays a crucial role in understanding the energy balance.

In this paper, we perform a detailed analysis of the Deep Impact energy balance. In particular, we estimate, to the extent possible, the amount and velocities of materials in the hot plume and in the ejecta. We also review the different physical processes associated with the impact event. Section 2 presents the Deep Impact data we used for our analysis. Section 3 gives the mass estimates derived for the different materials in the hot plume and the ejecta. Section 4 indicates the physical processes involved and their relative contribution to the energy balance. Finally, Section 5 contains a discussion of numerous issues involved in our analysis and our conclusions.

2. The data

The Deep Impact spacecraft took many images and spectra of the impact event using the MRI (medium resolution camera), HRI-VIS (high resolution camera) and HRI-IR (a 1–5 μm spectrometer that shares the HRI telescope) instruments (Hampton et al., 2005). From the images, A'Hearn et al. (2005) detected a self-luminous vapor plume (hereafter hot plume) in the first second after impact, followed by the development of a diffuse cone of fine (0.5–2.0 μm, Lisse et al., 2006; Sunshine et al., 2007) solid ejecta (hereafter ejecta or ejecta plume). In this paper, we mainly focus on the hot plume, which has not yet been studied in detail although it contains most of the energy released during the impact (Table 2). For global mass estimates of the ejecta plume, we rely on ground-based observations since the Deep Impact spacecraft was too close to the scene to make such measurements.

We use the three HRI-IR frames that include the hot plume: 9000041_010 (hereafter 1st frame), 9000041_011 (hereafter 2nd frame) and 9000041_12 (hereafter 3rd frame). The slit length is 64 pixels at this time (BINSF2 mode), which represents a total of about 180 spectra usable for science (excluding the two bad pixels on each edge). At the time of impact, the slit was at a fixed position relative to the nucleus center of mass, down range of the impact site. For the position of the slit relative to the impact site, we use MRI context images taken at the same time, but with a higher time

Table 2
Summary of the energy balance in the Deep Impact experiment.

Input	Mass (kg)				Kinetic (GJ)	Total energy (GJ)	Fraction of total input energy (%)
Impactor	372				19.7	19.7	>99.8
Total input energy						**19.7**	**100**
Output	Mass (kg)	Breakup and compression of aggregates (GJ)	Sublimation or melting (GJ)	Heating (GJ)	Kinetic (GJ)	Total energy (GJ)	Fraction of total output energy (%)
Hot plume							
H_2O	190 (+263/−71)		0.49 (+0.68/−0.18)	1.26 (+1.74/−0.47)	4.28 (+5.91/−1.60)	6.03 (+8.33/−2.25)	36.5
CO_2	1.6 (±0.5)		0.0009 (±0.0003)	0.0048 (±0.0015)	0.036 (±0.012)	0.042 (±0.013)	0.3
CO	8.2 (+11.3/−3.1)		0.0024 (+0.0033/−0.0009)	0.027 (+0.037/−0.010)	0.18 (+0.25/0.07)	0.21 (+0.30/−0.08)	1.3
Organics	27.9 (+25.0/−8.9)		0.023 (+0.020/−0.007)	0.21 (+0.19/−0.07)	0.63 (+0.56/−0.20)	0.86 (+0.77/−0.28)	5.2
Other volatiles	Negligible					–	–
Dust	255 (±128)		0.46 (±0.23)	0.59 (±0.29)	5.73 (±2.87)	6.8 (±3.4)	41.1
Ejecta							
H_2O	6.8×10^6 ($\pm 2.3 \times 10^6$)	1.49 (±0.50)			0.22 (±0.07)	1.71 (±0.57)	10.3
Other volatiles	Negligible					–	–
Dust	7.3×10^6 ($\pm 6.8 \times 10^6$)	0.09 (±0.07)			0.23 (±0.21)	0.32 (±0.28)	2.0
Impactor	372		0.08	0.48	Negligible	0.56	3.4
% of total output energy		9.5	6.4	15.6	68.5		
Total output energy						**16.5 (+9.1/−4.1)**	**100**

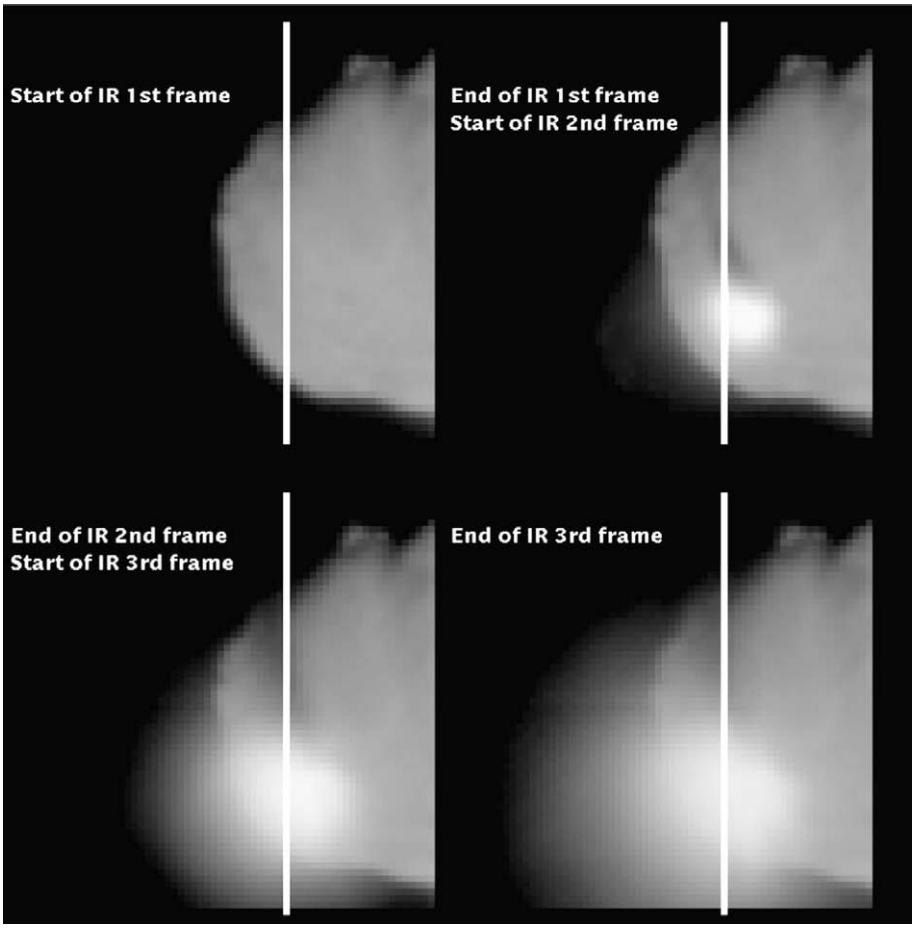

Fig. 1. Context images for the three HRI-IR frames used in this paper. We take the closest MRI image in time relative to the start and end of each HRI-IR frame. The white vertical lines correspond to the position of the HRI-IR slit relative to the MRI image, with pixel #0 located at the top of the line and pixel #63 at the bottom.

sample rate than HRI-IR, as illustrated in Fig. 1. The 1st IR frame started −0.4 s before impact and ended +0.3 s after impact. The 2nd IR frame started +0.3 s after impact and ended +1.0 s after impact. The 3rd IR frame started +1.0 s after impact and ended +1.7 s after impact. During this time, the spacecraft distance to the nucleus decreases from ∼8700 km to ∼8000 km. In the analysis of the MRI images presented in Schultz et al. (2007), the hot plume moved out of the HRI-IR field of view in less than 1 s after impact, so that all of the material in the hot plume is indeed captured in these three IR frames.

3. Mass estimates

To determine the energy budget of the event, we first need an estimate of the mass of the different materials present in the hot plume and the ejecta. This includes the volatiles such as H_2O, CO_2, CO, organic materials, dust and the impactor.

3.1. Hot plume

3.1.1. Water (H_2O)

Three rovibrational emission bands of water are visible in the hot plume spectra: the 1.4 μm, 1.9 μm and 2.7 μm band (Fig. 2). The 1.4 μm band is dominated by the (101-000) transition, the 1.9 μm band by the (011-000) transition and the 2.7 μm band by the (001-000) ν_3 transition. By default, we use the 2.7 μm band to estimate the amount of water, since it is the strongest band. When this band is saturated (which only happens in the 1st frame), we use the 1.4 μm band, which is then strong enough. We have also checked that when several bands are available, they all give the same amount of water molecules.

The observed infrared emission can come from two different sources: fluorescence emission due to the radiation of the Sun and thermal emission due to the temperature of the gas. As explained later, the gas is hot (900–1400 K) and fluorescence emission can be neglected (Table 1).

For thermal emission of H_2O, we can generate a synthetic spectrum using the following equation:

$$F(\lambda_i) = \frac{N_{mol}}{4\pi\Delta^2}\frac{g_{thermal}}{r_h^2}\frac{hc}{\lambda_i}\frac{1}{\alpha^2}\frac{1}{d\lambda_i} \quad (1)$$

where $F(\lambda_i)$ is the flux (W/m^2/μm/sr) in pixel i, N_{mol} is the number of molecules in the band, Δ (m) is the distance from the S/C to the comet, r_h is the heliocentric distance (AU), α (radian) is the pixel IFOV and $d\lambda_i$ (μm) the width of the pixel. We adjust N_{mol} and the temperature T of the gas to fit each observed spectrum. The g-factors values for thermal emission ($g_{thermal}$) have been derived from the HITRAN database.

The temperature of the gas is determined using the relative strength of the three water bands at 1.4 μm, 1.9 μm and 2.7 μm. The strength changes in a different way for each band as a function of temperature, so that we can determine the temperature that best matches the three bands for a given amount of molecules N_{mol}. Fig. 2 illustrates the results for the 1st IR frame; we derive a temperature of 1400 ± 100 K. In the 2nd and 3rd IR frame, the 1.4 μm and 1.9 μm bands are not visible, and only the 2.7 μm band is

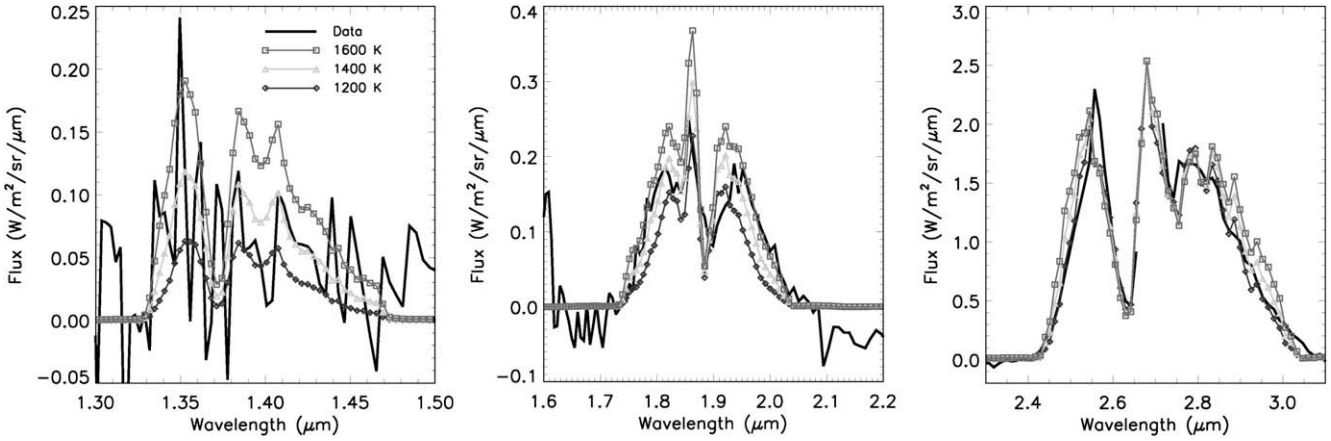

Fig. 2. Synthetic spectra superimposed on continuum subtracted data for the 1.4 μm (left panel), 1.9 μm (middle panel) and 2.7 μm (right panel) water bands in the 1st HRI-IR frame. The data correspond to the spectra of pixel #33 in Fig. 4. Each synthetic spectrum corresponds to a different gas temperature: 1200, 1400 or 1600 K. Only the spectrum at 1400 K fits the intensity of three water bands at the same time. The missing data between 2.65 and 2.70 μm are a combination of bad pixels and saturation.

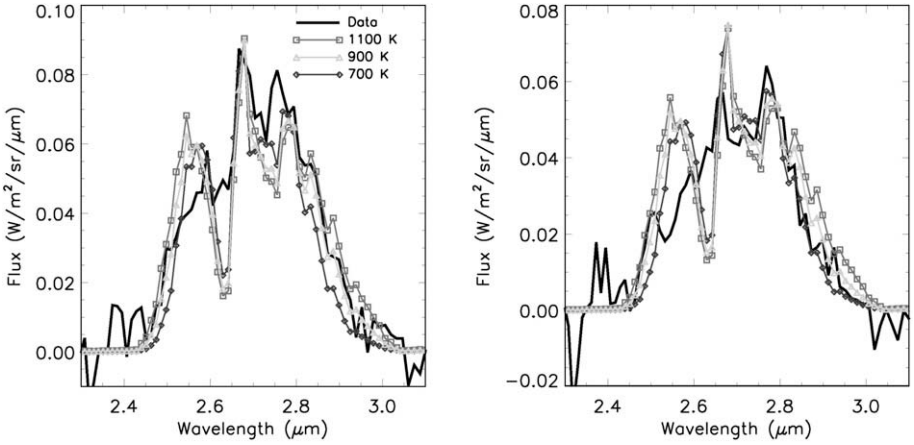

Fig. 3. Synthetic spectra superimposed on the continuum subtracted data for the 2.7 μm water band in the 2nd and 3rd HRI-IR frames. The data correspond to the spectra of pixel #33 in Fig. 4. Each synthetic spectrum corresponds to a different gas temperature: 700, 900 or 1100 K. The spectrum at 900 K gives the best fit to the water band using a chi-square method.

detected. As illustrated by Fig. 3, we used the width of this band to constrain the gas temperature to 900 ± 200 K. Once we know the temperature of the gas in the spectrum, we can derive the number of water molecules using Eq. (1) with the appropriated value for $g_{thermal}$, integrating the flux over the band width.

The final step is to take into account the fact that each water molecule does not spend the entire exposure time in the slit. The projected velocity of the gas is 5800 m s^{-1}, with a direction almost perpendicular to the slit (Schultz et al., 2007). At the time of observation, the spatial resolution of one slit pixel is 87 m, so that each molecule spends 87 m/5800 m s^{-1} = 0.015 s in the slit. The exposure time is 0.720 s, so that we have to multiply the amount of water molecules N_{mol} derived from Eq. (1) by 0.720 s/0.015 s = 48. But this is only valid for the 2nd and 3rd frames where the plume is in the slit for the entire exposure time. For the 1st frame, the plume only reaches the slit after 0.180 s (according to MRI images), which gives an effective exposure time 0.540 s for the plume and a multiplicative factor of 36 (0.540/0.015). Fig. 4 illustrates the final results with N_{mol} (×36 for the 1st frame and ×48 for the 2nd and 3rd frames) as a function of pixel number in the slit (spatial dimension), for the three frames containing the hot plume. The 1st frame contains most of the hot plume water molecules (5.1×10^{27} molecules), about one order of magnitude more than the 2nd (9.4×10^{26} molecules) and 3rd (3.3×10^{26} molecules) frames. If

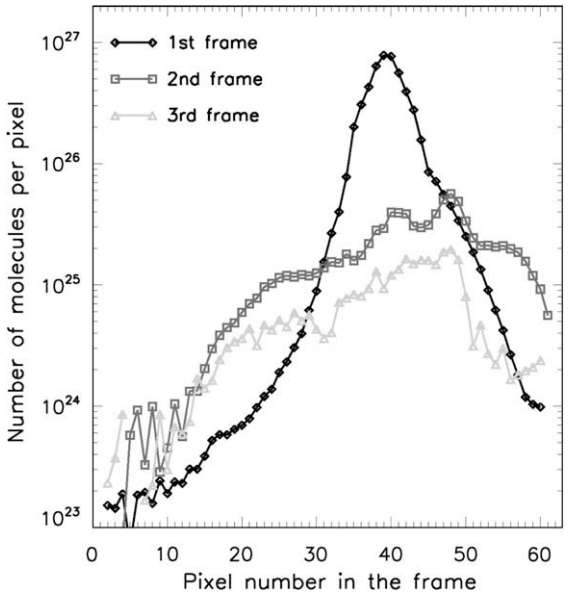

Fig. 4. Number of H_2O molecules per pixel in the hot plume, as a function of pixel number in the slit, for the first three HRI-IR frames.

we extrapolate this trend to the following frames, this confirms that the plume is almost entirely (~97%) captured in these three frames and dominantly (>80%) in the 1st one. The distribution has also a maximum around pixel #39, consistent with the context MRI images (Fig. 1), and indicating a good positioning of the slit relative to the hot plume to study it.

From the number of H_2O molecules in each pixel, we derive the column density. This requires the instantaneous amount of molecules in the slit (N_{mol}), and not the integrated amount as illustrated in Fig. 4 ($N_{mol} \times 36$ or $\times 48$). At a distance of 8680 km and a pixel size of 10^{-5} radian, the pixel size is 7534 m^2. The column density can be translated into opacity τ_{ul} using Eq. (2) from Crovisier (2006):

$$\tau_{ul} = \frac{c^2}{8\pi\nu^2}\frac{w_u}{w_l}A_{ul}\frac{Z_l(T)}{Z_{tot}(T)}\frac{N_{species}}{\Delta\nu} \quad (2)$$

where $N_{species}$ is the column density, ν is the line frequency, w_u and w_l are the upper-state and lower-state statistical weight, A_{ul} is the Einstein coefficient, $Z_l(T)$ is the energy distribution of the lower-state, $Z_{tot}(T)$ is the partition function, T is the rotational temperature and $\Delta\nu$ is the line width. We used a line width $\Delta\nu = 1$ km s^{-1}, which corresponds to 3.75×10^8 Hz for 2.7 μm, 5.32×10^8 Hz for 1.9 μm and 7.25×10^8 Hz for 1.4 μm. We calculated the opacity for each pixel and obtained maximum line opacity of 0.44 for the 2.7 μm band and 0.03 for the 1.4 μm band. With opacities below one, we conclude that all of the water lines are optically thin in all of the spectra. We note that for high temperature (thermal regime), lines become optically thick for larger values of columns densities than for low temperature (fluorescence regime), because the partition function is much larger.

Finally, we obtain a total of 6.4 (+8.8/−2.4) $\times 10^{27}$ molecules of water vapor in the hot plume, or 190 (+263/−71) kg, with 152 kg in the first frame, 28 kg in the second frame and 10 kg in the third frame. Error bars come from the calibration of the HRI-IR instrument (10%) and g-factors due to temperature uncertainties (Table 1).

3.1.2. Carbon dioxide (CO_2)

The CO_2 band detected with the HRI-IR spectrometer is the 4.3 μm band (ν_1) (Fig. 5). We estimate the total number of molecules and mass of gas as done for H_2O. The g-factors are given in Table 1, and here again the thermal emission is the dominant process. CO_2 is only detected in the 1st IR frame. As illustrated in Fig. 5, the fit between the synthetic and the observed spectrum is not very good, and we cannot use the width of the CO_2 band to determine its temperature. Instead, we assume the same temperature as for H_2O, which is 1400 K. To adjust the synthetic spectra to the observed one, we ensure that the integrated signals of both are equal.

The mismatch between the synthetic and the observed spectrum cannot simply be a temperature effect. For a low temperature of 200 K, the width of the band is too small to fit the data. For high temperature (900–2000 K), the width of the band is larger, and the fit to the data is better. But the shape of the CO_2 band shows a strong double peak, not compatible with the data at our spectral resolution and not located at the correct expected wavelength. Finally, we have also investigated the possible role of $^{13}CO_2$. It adds a third peak to the spectra around 4.38 μm, which helps to fit the data better, but only for unrealistic values of $^{12}CO_2/^{13}CO_2 < 10$, while typical values for comets are in the range 90–165 (Bockelée-Morvan et al., 2004). So, although we believe the 4.3 μm region is dominated by CO_2 emission lines, we currently do not have a satisfactory explanation for the exact shape of the synthetic spectrum, and this point would need further investigations. If other molecules are present in the 4.2–4.4 μm region, our estimate could possibly be overestimated.

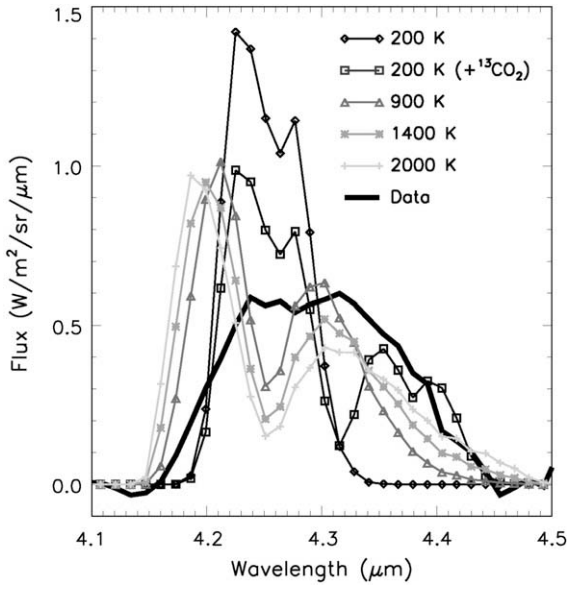

Fig. 5. Synthetic spectra of CO_2 for different temperatures (200, 900, 1400 and 2000 K), superimposed to an observed spectrum (continuum subtracted). The possible contribution of $^{13}CO_2$ is also evaluated but rejected since it gives unrealistic values of $^{12}CO_2/^{13}CO_2$ (see text for details).

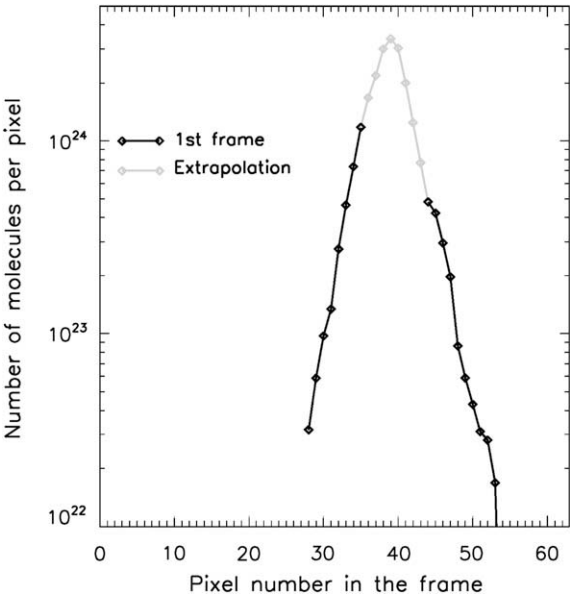

Fig. 6. Number of CO_2 molecules per pixel present in the hot plume, as a function of pixel number in the slit, for the 1st HRI-IR frame. The amount of CO_2 molecules in the other frames is negligible. Because of the saturation limit of the HRI-IR instrument, we performed an extrapolation around the maximum, assuming the same behavior as H_2O in Fig. 4.

From Eq. (2), we calculate a maximum line opacity of 0.1, so that the CO_2 band is optically thin. Fig. 6 illustrates the amount of CO_2 molecules in the hot plume, as a function of pixel number (spatial dimension). Close to the maximum (around pixel #39), the data were saturated, and we did an extrapolation assuming the same behavior as H_2O in Fig. 4. Finally, we derive an amount of CO_2 molecules in the hot plume of $2.2 \pm 0.7 \times 10^{25}$ molecules, or 1.6 ± 0.5 kg.

3.1.3. Carbon monoxide (CO)

The CO emission lines at 4.6 μm were not detected in the HRI-IR spectrometer because of calibration issues beyond 4.5 μm.

However, CO has been observed on Comet 9P/Tempel 1 during the Deep Impact encounter (Mumma et al., 2005), and may, therefore, be present in the hot plume. By lack of data to estimate the CO abundance relative to water in the hot plume, we use the value of 4.3% derived by Mumma et al. (2005) for the bulk composition. This translates to a CO mass estimate of 8.2 (+11.3/−3.1) kg.

3.1.4. Organic materials

Organic materials are detected by the HRI-IR instrument, as illustrated by the Gaussian distribution of organic emission lines in the 3.2–3.6 μm region (Fig. 8). Although we cannot identify which organics were detected, we know from other comet observations that the main molecules in this region should be CH_3OH, CH_4, C_2H_6 and H_2CO (Bockelée-Morvan et al., 2004). The $g\odot$ factors given in Table 1 were obtained by adding the $g\odot$ for these molecules (Coradini et al., 1998). The value of $g_{thermal}$ is unknown because we do not know exactly which organic molecules we have and how they behave at high temperature (especially CH_3OH). As a first approximation, we use a $g_{thermal}$ value ∼10 times lower than that of CO_2, since organic molecules have comparable $g\odot$-factors and partition functions up to ∼10 times larger (for CH_3OH). This is a strong assumption but, as we shall see later, the implications for the energy budget are small. The organics are detected in the first three frames, but we cannot determine their temperature. We, therefore, used that of H_2O, which is 1400 K in the 1st IR frame and 900 K in the 2nd and 3rd IR frame.

We integrated the flux in the 3.2–3.6 μm band and used Eq. (1) with the appropriated value for $g_{thermal}$ to derive the amount of organic molecules. Results are illustrated by Fig. 7. The maximum column density is 10 times larger than that of CO_2, but with a partition function 10 times larger, we can confidently assume that the organics lines are optically thin. As for CO_2, close to the maximum (around pixel #39), the data were saturated, and we did an extrapolation assuming the same behavior as H_2O in Fig. 4.

Finally, we obtain a total of 6.2 (+5.6/−2.0) × 10^{26} molecules of organics in the hot plume, or 27.9 (+25.0/−8.9) kg, with 19.4 kg in the first frame, 7.7 kg in the second frame and 0.7 kg in the third frame. We have used a molecular mass of 27 g/mole, the mean of the molecular mass of CH_4, CH_3OH, C_2H_6 and H_2CO.

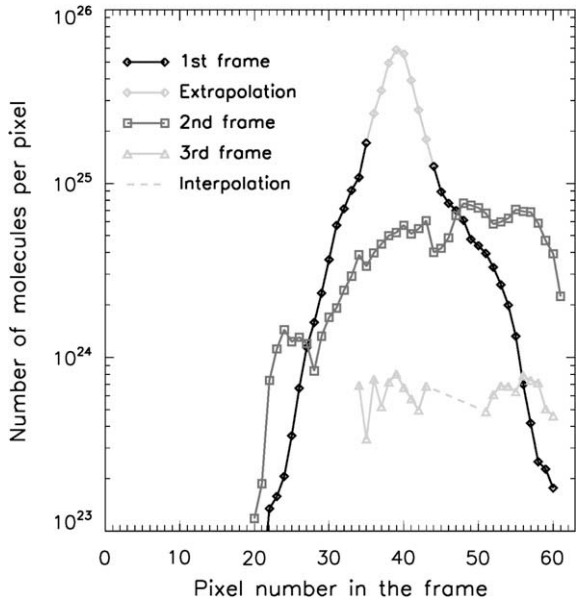

Fig. 7. Number of organic molecules per pixel present in the hot plume, as a function of pixel number in the slit, for the first three HRI-IR frames. Because of the saturation limit of the HRI-IR instrument, we performed an extrapolation around the maximum in the 1st frame, assuming the same behavior as H_2O in Fig. 4.

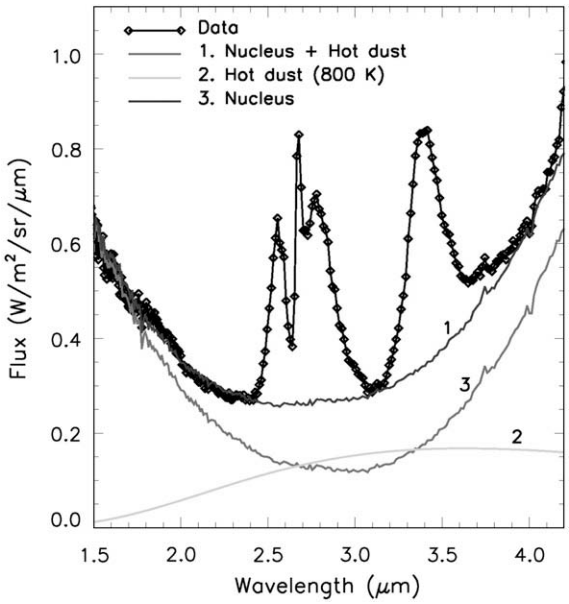

Fig. 8. Deep Impact spectrum of the hot plume, corresponding to pixel #33 in Fig. 4. The continuum is well fitted with a contribution of the pre-impact nucleus and hot dust at 800 K. There is a strong emission of water at 2.7 μm and organic molecules at 3.4 μm.

3.1.5. Dust

The mass of dust in the hot plume can be derived from the continuum in the three HRI-IR frames. The result depends on several parameters: grain radius, grain temperature, filling factor and the contribution of the nucleus to the background. We have estimated for each spectrum the combination of these parameters that best fits the data, using a chi-square method. Fig. 8 illustrates the results for one spectrum, with a dust temperature of 800 K, a filling factor of 1.2 × 10^{-4}, a nucleus contribution of 80% and a grain size of 10 μm. For the nucleus spectrum, we used the value just before impact, since the slit was pointing at the same location.

We repeated this procedure for each spectrum of the hot plume to obtain the filling factor as a function of pixel number (spatial dimension). The mass of dust M can be derived from the number of dust grains N, assuming a density ρ and a grain radius r: $M = N4/3\pi r^3\rho$. The number of dust grains can be derived from the emitting surface S in one pixel (87 × 87 m^2), the filling factor F and the grain size: $SF = N\pi r^2$. As for the gas, this number has to be multiplied by $\gamma = 36$ (1st frame) or $\gamma = 48$ (2nd frame) to take into account the velocity of the dust across the slit. Finally, we obtain: $M = \gamma SF4/3r\rho$. Fig. 9 illustrates the result with the mass in each pixel of the first two IR frames, assuming a grain radius of 10 μm and a grain density of 1000 kg/m^3. We obtain a total of 255 ± 128 kg of dust in the plume, with 223 kg in the first frame and 32 kg in the second one. The amount of hot dust is negligible in the third frame. We used an uncertainty of 50% on the mass, which we believe is conservative. This results from the uncertainties in the filling factor, the contribution of the nucleus to the background and the grain temperature. The above mass estimate depends strongly on the assumed grain radius and density. Larger grains (>10 μm) or density (>1000 kg/m^3) would imply a larger mass of dust, while smaller grains or a lower density would imply a smaller mass. Richardson et al. (2007) estimated the bulk density of the nucleus to 400 kg/m^3. The value for the individual grains may be larger, so 1000 kg/m^3 was assumed in order to be conservative.

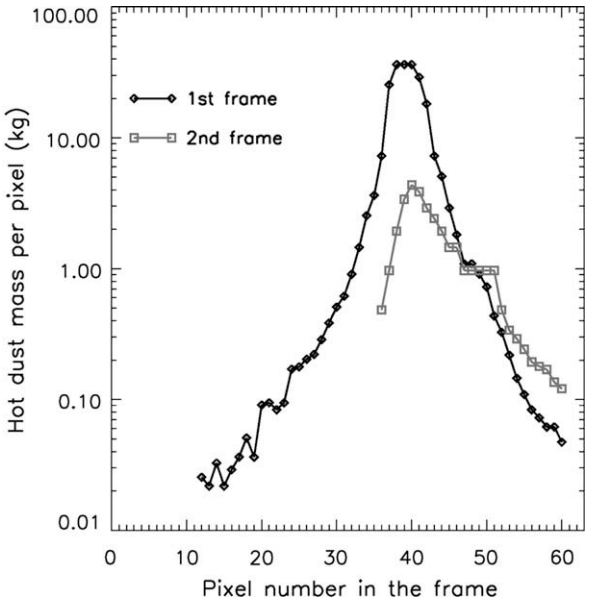

Fig. 9. Amount of dust in the hot plume per pixel, assuming a grain radius of 10 μm and a grain density of 1000 kg/m^3, for the first two HRI-IR frames. The amount of dust in the 3rd frame is negligible.

Sunshine et al. (2007) derived a radius of 1 μm for the icy grains in the ejecta, and Sunshine et al. (2006) derived a radius of 10 μm for the icy grains on the surface of the nucleus. According to Jorda et al. (2007), dust grains with radii <10 μm contribute to more than 85% of the cross-section of the ejecta. So, our assumption of 10 μm for the dust grain radius in the hot plume seems realistic as an upper limit. However, the grains detected in the hot plume have been melted, and their size distribution may be different of that in the ejecta. Based on the brightness decrease in the hot plume in the first second after impact, resulting from the cooling of the grains and reflected sunlight, Melosh (2006) estimated a grain radius of 160 μm, with a density of 2500 kg/m^3, an albedo of 0.1 and an initial temperature of 3500 K. With a grain radius of 10 μm as used above, the same cross-section (brightness) will imply a mass 15 times smaller, which is 270 kg, in very good agreement with our dust mass determination. In this case the cooling rate would be faster, but may still be compatible with the hot plume brightness decrease in the first second. Further analysis of this issue goes beyond the scope of this paper.

Schultz et al. (2007) made a first-order estimate that the total amount of vaporized materials released by the DI experiment was 3–5 times the mass of the impactor (about 1100–1860 kg). This estimate came from the assumption that 10% of the impactor energy was partitioned into the internal energy of the expanding vapor plume based on experiments using nominal density particulate targets. Schultz et al. (2007) and Ernst and Schultz (2007) also conclude, however, that the evolution of the ejecta and the impact flash indicate an under-dense target. Such a target would significantly reduce the assumed partitioning from 10% to 1–2%, yielding results more consistent with values derived here.

3.2. Ejecta

Following the generation of the hot (self-luminous) plume in the first 2 s, a large amount of material was excavated. This material, composed of fine dust grains and volatiles, forms the ejecta. While the hot plume contains a small mass (<10^3 kg) traveling at high velocity (>5.8 km/s), the ejecta contains a large mass (>10^6 kg) traveling at a low velocity (<10 m/s).

3.2.1. Volatile materials

Keller et al. (2007) have estimated the production of water molecules released by the impact as $6.8 \pm 2.3 \times 10^6$ kg. Other volatile molecules in this component, like CO_2, CO or organic molecules, are negligible for the energy balance since their abundance relative to water is lower than 7% for Comet 9P/Tempel 1 (e.g., Mumma et al., 2005; Feaga et al., 2007).

3.2.2. Dust

The total amount of dust ejecta released by the Deep Impact experiment is not very well constrained. Sugita et al. (2005) reported $5.6–8.5 \times 10^5$ kg, Keller et al. (2007) reported 7×10^6 kg, Jorda et al. (2007) reported $1 \times 10^6–1.4 \times 10^7$ kg and Lisse et al. (2006) reported $>8 \times 10^6$ kg. This discrepancy mainly arises from the unknown parameters mentioned in Section 3.1.5. Overall, the amount of dust in the ejecta is $7.3 \pm 6.7 \times 10^6$ kg. Compared to this amount, the mass of the hot plume is negligible (<0.01%).

3.3. Other materials

For an oblique impact onto a porous target as in the case of Deep Impact, the impactor is catastrophically disrupted into fragments that are then melted and dispersed at shallow depth (Schultz et al., 2005). As a consequence, material from the impactor was not likely to be present in the hot plume, but may have contributed to the ejecta plume. However, it must have been heated and melted during the impact, which must be taken into account in the detailed reckoning of the energy balance. The kinetic energy of the impactor fragments in the ejecta can be ignored since the mass of the impactor (372 kg) is negligible compared to the mass of the dust ejecta ($7.3 \pm 6.7 \times 10^6$ kg).

Other volatile molecules like for example HCN, NH_3 or H_2S could also be present in the hot plume and the ejecta, but we can ignore them since their abundance relative to water, in the case of a Jupiter Family comet like 9P/Tempel 1, is typically <<1%.

4. The energy balance

Now that we have determined the different materials involved in the impact process and calculated their mass, we can focus on the different physical processes undergone by these materials. Due to the shock and friction, materials in the hot plume were *heated* and then *cooled* by expansion and radiative loss. At the high temperatures that were achieved in the impact, volatiles were *sublimated*, and refractory materials were *liquefied*. The shock propagating into the surface layers also probably changed the nature of the dust and ice aggregates: they were *compressed* and/or *broken up* into smaller pieces. A fraction of the materials surrounding the impact site were also probably *heated*. Water ice, if present in its amorphous phase before impact, would have been *crystallized*. Finally, and most importantly, materials were excavated from the surface, therefore *accelerated*, and gained kinetic energy. Crystallization and cooling are exothermic processes, while all the other processes are endothermic. For the energy balance, we divide the processes into two categories: (i) input energy for the processes that add energy to the system and (ii) output energy for processes that extract energy. Results for all these processes are given in this section and summarized in Table 2.

4.1. Input energy

The input energy mainly comes from the kinetic energy of the impactor. For a mass of 372 kg and a velocity 10.3 km/s, we have a kinetic energy of 19.7 GJ. The crystallization of water ice, in case it was in amorphous phase before the impact, may also add some

energy to the system. However, amorphous ice is unstable and crystallizes in a few days for temperature above 120 K (Schmitt et al., 1989). With a maximum surface temperature above 300 K at the impact site (Groussin et al., 2007), a heat wave that penetrates of 0.9 m into the nucleus per orbital period for Comet 9P/Tempel 1 (Sunshine et al., 2007), and a perihelion distance between 2.0 and 1.5 AU for at least the last 50 orbits (Yeomans et al., 2005), we calculate that the temperature is above 120 K in the first meters of depth, effectively excluding the presence of amorphous ice in the immediate sub-surface region. The crystallization of water ice should extend from this surface zone down to the furthest depth (10–30 m) of the Deep Impact excavation, due to runaway process of exothermic crystallization (Prialnik et al., 2004).

4.2. Output energy

4.2.1. Heating and cooling of materials

We measured a maximum temperature of 1400 K for the gas in the hot plume and 800 K for the dust, but this temperature was measured 100s of milliseconds after impact and is not representative of the temperature at the time of impact, which changed quickly in the first seconds. The temperature reached at impact could be as high as 3500 K according to Melosh (2006). Then, according to the same author, the hot plume cooled down very rapidly, from 3500 K to 1000 K in only 420 ms. Assuming an initial temperature of 200 K close to the surface (lower limit, Groussin et al., 2007), this implies heating of 3300 K for all materials in the hot plume. Since we have no information for the temperature reached by the impactor during the collision, we will also assume 3500 K, which is, however, probably an upper limit.

For H_2O, heating requires an energy of 1.26 (+1.74/−0.47) GJ, assuming a gas heat capacity of 2.0 kJ/K/kg. For CO_2, an energy of 0.0048 ± 0.0015 GJ is required, assuming a gas heat capacity of 0.9 kJ/K/kg. For CO, an energy of 0.027 (+0.037/−0.010) GJ is required, assuming a gas heat capacity of 1.0 kJ/K/kg. For the organic material, an energy of 0.21 (+0.19/−0.07) GJ is required, assuming a gas heat capacity of 2.3 kJ/K/kg, the mean of 2.5 kJ/K/kg for CH_4 and C_2H_6 and 1.9 kJ/K/kg for CH_3OH. For the dust, an energy of 0.59 ± 0.29 GJ is required, assuming a solid heat capacity of 0.7 kJ/K/kg (silicate). For the impactor material, an energy of 0.48 GJ is required, assuming a solid heat capacity of 0.39 kJ/K/kg (copper). Volatiles and refractory materials present in the ejecta were not significantly heated by the impact process but mainly by the Sun (Groussin, 2005), which is not part of this energy balance. Finally, we note that Schultz et al. (2007) derived a slightly higher temperature of ∼3900 K for the hot plume by comparison to laboratory experiments, however, this difference would only increase the heating energy by 10% and the total output energy by less than 2%.

After its initial heating to 3500 K at impact, the plume materials were rapidly cooled to 1400 K (volatiles) and 800 K (dust) by the time we observed them. This adds some energy to the system due to expansion and radiative loss. However, this energy is only available *after* the initial heating to 3500 K and is not part of this energy balance. It can be used to accelerate plume materials (see Section 5). Using the earlier mentioned heat capacity values, we calculate that the cooling of the plume liberates a total of 1.3 GJ, with 0.8 GJ from volatiles and 0.5 GJ from the dust.

Sub-surface materials surrounding the impact site and not excavated in the hot plume were probably heated during the impact process. The energy required to heat these materials can only be estimated using numerical simulations since it was not observable by the Deep Impact instruments. For an impact on a porous target like 9P/Tempel 1, heating is restricted to a thin surface layer (Belyakov et al., 1978). From hydrocode modeling and for a 10 km diameter asteroid impacting the Earth at 20 km/s (Chicxulub crater), Pierazzo and Melosh (1999) estimated the increase in temperature to about 200 K. No simulations are currently available for highly porous targets. For Deep Impact, this number is lower since the density of 9P/Tempel 1 is 10 times lower than that of the Earth (the shock wave quickly dissipates with compression), and that the impact velocity is only 10.2 km/s. With a more realistic assumption of an increase of 100 K in temperature for the materials surrounding the impact site and not excavated in the hot plume, and assuming that heating affects a region corresponding to 10 impactor volume, an energy of 0.03 GJ is required, which can be neglected as it represents 0.15% of the total input energy.

4.2.2. Sublimation and melting of materials

The high temperature reached at impact, 3500 K, implies that all materials present in the hot plume would have been sublimated (volatiles) or melted to glowing droplets (refractory materials). Evaporation of refractory materials can be neglected as they cool down faster than the time it takes to vaporize them (Melosh, 2006), and, moreover, the net result of vaporization followed almost instantaneously (<200 ms) by condensation is null in terms of energy balance. For H_2O, sublimation requires an energy of 0.49 (+0.68/−0.18) GJ, assuming a latent heat for sublimation of 2591 kJ/kg. For CO_2, an energy of 0.0009 ± 0.0003 GJ is required, assuming a latent heat for sublimation of 572 kJ/kg. For CO, an energy of 0.0024 (+0.0033/−0.0007) GJ is required, assuming a latent heat for sublimation of 293 kJ/kg. For organic material, an energy of 0.023 (+0.020/−0.007) GJ is required, assuming a latent heat for sublimation of 809 kJ/kg, the mean values of C_2H_6 = 615 kJ/kg, CH_4 = 613 kJ/kg and CH_3OH = 1199 kJ/kg (we could not find a value for H_2CO, but it has a negligible impact in the energy balance). For the dust, an energy of 0.46 ± 0.23 GJ is required, assuming a liquefaction (melting) energy of 1800 kJ/kg (silica). For the impactor, an energy of 0.08 GJ is required, assuming a liquefaction energy of 209 kJ/kg (copper).

Volatiles (mainly water) present in the ejecta plume were sublimated using solar energy and not the kinetic energy of the impactor, so they should not be part of the energy balance. This point is justified as follows. The water mass estimate in the ejecta derived by Keller et al. (2007) is based on observations performed many (10–100) hours after the impact event, when the ejecta was in thousands of km from the nucleus. But after 45 min, Sunshine et al. (2007) demonstrated that water ice is only detected a few kilometers away from the nucleus, so that all icy grains at further distance have been sublimated. Moreover, sub-micron icy grains, as detected in the ejecta (Sunshine et al., 2007) would sublimate in a few hours (Patashnick and Rupprecht, 1977) before the OSIRIS observations of Keller et al. (2007). Finally, we calculate that sublimating all the water in the ejecta plume requires about 17,000 GJ, about three orders of magnitude more than the kinetic energy of the impactor (19.7 GJ), so that a massive external source of energy is obviously required, i.e., the Sun.

4.2.3. Kinetic energy

The projected velocity of the hot plume is 5800 m/s, in a direction almost perpendicular to the slit. Comparing the MRI images to the simulations of Richardson et al. (2007), we estimate that the hot plume is about 30° out of the plane of sky, which gives a deprojected velocity of 6700 m/s for the materials in the hot plume.

The velocity of the leading edge of the ejecta was estimated by ground-based observers as 200 ± 20 m/s (Meech et al., 2005). However, as explained by Richardson et al. (2007), the leading edge only represents the "tip of the iceberg" such that the majority of particles were ejected at speeds of one to three orders of magnitude below this value. This effect is also confirmed by Holsapple and Housen (2007). Moreover, as demonstrated by Keller et al.

(2007), the gas release by sublimation in the vicinity of the nucleus will very efficiently accelerate micron size dust particles to speeds of 100s of m/s. As a consequence, the observed velocity and kinetic energy of the dust in the ejecta plume are not linked to the kinetic energy of the impactor but mostly to the sublimation energy of water ice grains due to solar radiation. For a total amount of materials excavated $>10^6$ kg, Richardson et al. (2007) gives an upper limit of 10^3 Pa for the surface strength. With this strength, they estimate that >80% of the particles have an ejection velocity <2 m/s. More precisely, we calculate that their mass vs. velocity distribution (their Fig. 9, right panel) in the ejecta plume has the same kinetic energy as the same ejecta mass moving at a constant velocity of about 8 m/s. We use this value of 8 m/s as our best estimate of the mean ejecta velocity.

With the above values for the velocity of the hot plume and the material in the ejecta, we can calculate the kinetic energy of the different components. For H_2O in the hot plume, we obtain a kinetic energy of 4.28 (+5.91/−1.60) GJ. For CO_2 in the hot plume, we obtain 0.036 ± 0.012 GJ. For CO in the hot plume, we obtain 0.18 (+0.25/−0.07) GJ. For the organics in the hot plume we obtain 0.63 (+0.56/−0.20) GJ. For the dust in the hot plume, we obtain 5.73 ± 2.87 GJ. For the dust in the ejecta, we obtain 0.23 ± 0.21 GJ. Finally, for H_2O in the ejecta, we obtain a kinetic energy of 0.22 ± 0.07 GJ.

4.2.4. Compressing and breaking dust and ice aggregates

During the impact process, dust and ice aggregates are likely to have been compressed and/or broken into smaller pieces. The dust ejecta is dominated by sub-micron grains of 0.5–1.0 μm radius (Meech et al., 2005). As mentioned in A'Hearn et al. (2005), those grains preexisted either as very fine particles or as weak aggregates of such particles. Unfortunately, there are no estimates of the dust grain radius on the surface before impact. However, there is an evidence for a possible break up of aggregates coming from water ice. The water ice exposed on the surface is composed of 10 μm grains (Sunshine et al., 2006), while the water ice grains in the ejecta plume are sub-micron in radius (Sunshine et al., 2007), indicating fragmentation of the grains due to impact. In any case, if there has been compression and/or fragmentation of grains, this must be investigated in terms of energy.

The cohesion and fragmentation of grain aggregates have been studied in detail by Dominik and Tielens (1997). From their results, we can estimate the energy required to compress or break an aggregate composed of micron size particles. From Table 2, the dust ejecta mass is $7.3 \pm 6.7 \times 10^6$ kg, and the water (gas) ejecta mass is $6.8 \pm 2.3 \times 10^6$ kg. It is difficult to estimate the amount of water observed in gas phase after impact that was in solid phase before impact. To be conservative, we assume that all the water gas was in solid phase before impact. This gives an upper limit on the amount of water ice. Assuming a bulk density of 400 kg/m^3 (Richardson et al., 2007), this corresponds to a volume of $1.8 \pm 1.7 \times 10^4$ m^3 for the dust and $1.7 \pm 0.6 \times 10^4$ m^3 for the ice. For micron size particles (Meech et al., 2005; Sunshine et al., 2007), this translates to $4.3 \pm 4.1 \times 10^{21}$ particles of dust, and $4.1 \pm 1.4 \times 10^{21}$ particles of water ice. From Dominik and Tielens (1997), the energy required to break one bond between such particles is about 1.8×10^{-15} J for graphite (the closest analog to silicate in their paper) and 3.4×10^{-14} J for water ice. Assuming that, on average, each particle is connected to two others to form an aggregate, the minimum energy required to break all the bonds is 0.008 ± 0.007 GJ for dust and 0.135 ± 0.045 GJ for water ice. This energy also corresponds to the maximum possible compression of the aggregates before they break. In practice, the amount of energy required to really break an aggregate is ∼10 times larger, and this refers to what Dominik and Tielens (1997) call the catastrophic disruption of the aggregate.

Overall, assuming that all aggregates in the ejecta (dust and ice) were broken into small pieces in a catastrophic disruption, and that a volume equivalent to the excavated one was compressed to its maximum in the layers surrounding the impact, a total energy of 1.6 ± 0.6 GJ is required. But this is an upper limit since, in all probability, only a fraction of the aggregates were catastrophically disrupted or compressed to maximum.

5. Discussions and conclusions

Our results on the energy balance of the Deep Impact experiment are summarized in Table 2 and Fig. 10. With an input energy of 19.7 GJ and an output energy in the range 16.5 (+9.1/−4.1) GJ, the balance is, within the uncertainties, in equilibrium. The error bar on the output energy mainly comes from the uncertainty on the water and dust mass estimates. From our analysis, we obtain 190 (+263/−71) kg of water in the hot plume, 1.6 ± 0.5 kg of CO_2 in the hot plume, 8.2 (+11.3/−3.1) kg of CO in the hot plume, 27.9 (+25.0/−8.9) kg of organic materials in the hot plume and 255 ± 128 kg of dust in the hot plume. In addition, ground-based observers derived $6.8 \pm 2.3 \times 10^6$ kg of water in the ejecta, and $7.3 \pm 6.7 \times 10^6$ kg of dust in the ejecta plume (see Section 3.2).

Most of the energy (85%) goes into the hot plume (mainly for dust and water), which only represents a very small fraction (<0.01%) of the total ejected mass. About 12% of the energy goes into the ejecta (mostly water) and 3% to destroy the impactor. Other volatiles species like CO_2, CO and organic material contribute 0.3%, 1.3% and 5.2% to the energy balance respectively, so their contribution is small compared to water. Since ground-based observations only detect the ejecta material, it illustrates the importance of the images taken at high cadence by the Deep Impact spacecraft that detected the hot plume: only three HRI-IR frames and a few tens of MRI and HRI-VIS images. These were all taken in the first 2 s after impact and cover 85% of the energetic processes.

In terms of physical processes, 68% of the energy is used to accelerate grains (kinetic energy), 16% to heat them, 6% to sublimate or melt them and 10% (upper limit) to break or compress dust and water ice aggregates into small micron size particles. Schultz et al. (2007), comparing Deep Impact and laboratory impact experiments, estimated that ∼37% of the energy should go into vaporization (heating, melting and sublimation) based on experiments using solid water–ice targets. This contrasts with our estimate of 22% (16 + 6%). This discrepancy likely reflects the low density of the pre-impact target materials indicated by the evolution of the ejecta and impact flash (Schultz et al., 2007; Ernst and Schultz, 2007). Experiments with under-dense targets indicated reduced coupling efficiency resulting in a much lower (×5–10) estimate for the partitioning into internal energy and the vaporized mass fraction. This further reinforces the need for laboratory experiments which are fundamental and invaluable to understand the physics. The dust in the ejecta does not contribute significantly to the energy balance with only 2.0% of the output energy. As explained in Section 4.2.1, the cooling of the hot plume liberates 1.3 GJ of energy, which corresponds to ∼10% of the kinetic energy of the plume (Table 2). This translates to a decrease of ∼400 m/s in our estimate of the velocity of plume material (6300 m/s instead of 6700 m/s). This would correspond to a change of only 6° on the projected angle (24° instead of 30°), and for this reason, we consider that it is well within the error bars.

Since the emission lines are optically thin in the hot plume (due to the high temperature), we can use our mass estimates as a proxy for the nucleus composition at the impact site. Based on laboratory experiments on porous targets, Schultz et al. (2007) show that materials in the Deep Impact hot plume come from the upper layers of a few projectile diameters in depth. We obtain a dust/H_2O

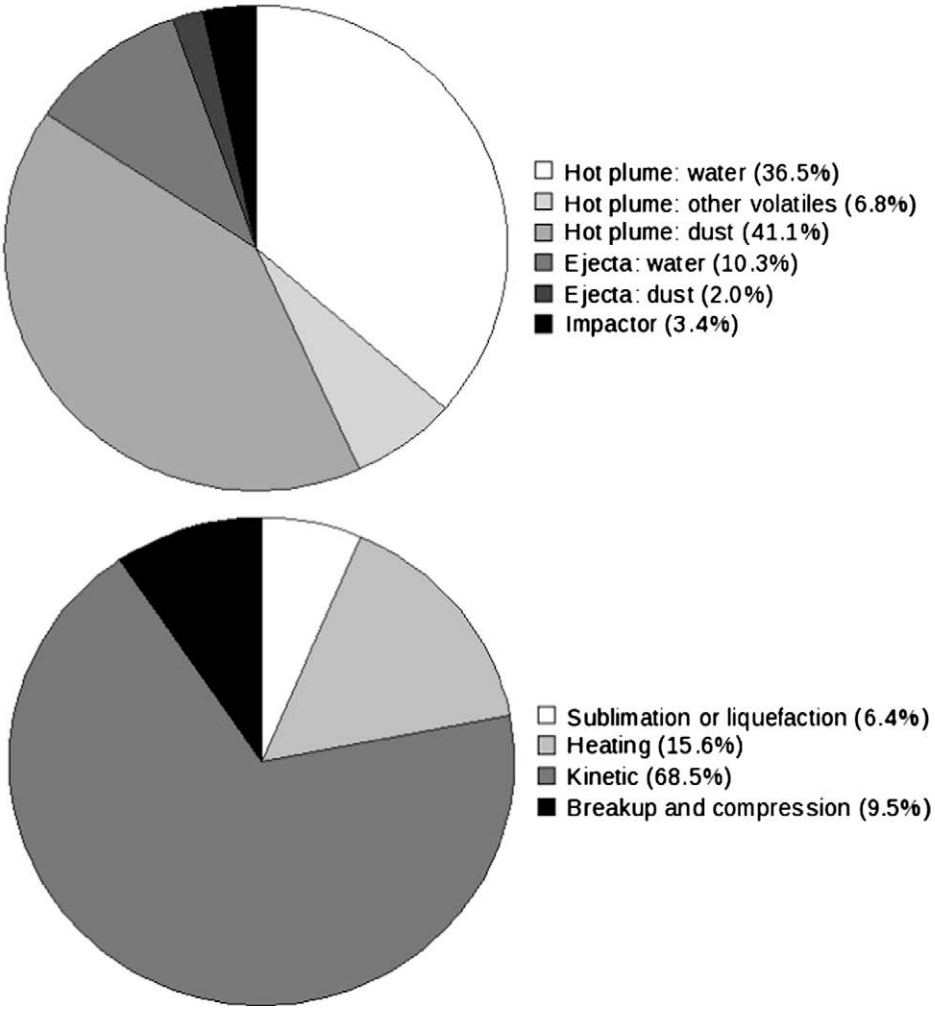

Fig. 10. (top panel) Distribution of the energy in the Deep Impact experiment between the different components (hot plume, ejecta, impactor) and (bottom panel) the physical processes.

ratio of 1.3 (+1.9/−1.0), a CO_2/H_2O ratio of 0.008 (+0.009/−0.006) and an organics/H_2O ratio of 0.15 (+0.29/−0.11). This is quite different from estimates of the average composition of Comet 9P/Tempel 1 before impact. The dust to gas ratio is larger than the average value of about 0.5 measured by Lisse et al. (2005), the organics/H_2O ratio is larger than the average value of about 0.02 measured by Mumma et al. (2005) before impact, and the CO_2/H_2O ratio is lower than the average value of 0.07 determined by Feaga et al. (2007) before impact. However, as observed by Farnham et al. (2007) and Feaga et al. (2007), there are large asymmetries in the dust and gas spatial distribution in the coma, so that the composition at the impact site may not be representative of that of the nucleus. These asymmetries could result from the different surface layers observed by Thomas et al. (2007). In particular, since the impact site is located close to the equator, near 25°S, it experiences a strong insolation close to perihelion, and the enhancement of H_2O in the sunward direction observed by Feaga et al. (2007) can be easily explained. Following this argument, it is likely that the upper layers of the impact site could be depleted in H_2O and even more so in CO_2 (and CO) which is more volatile. This could explain the large dust/H_2O ratio and the low CO_2/H_2O ratio. Finally, as proposed by A'Hearn et al. (2005), the enhancement in organic materials in the hot plume compared to ground-based observations of the cold ejecta suggests that we may be vaporizing organics that would not normally be vaporized in comets. In this sense, the organics/dust ratio of 0.11 (+0.30/−0.07) for the hot plume, derived from Table 2, should be a good estimate for Comet 9P/Tempel 1. This is an intermediate value between the ∼3%wt carbon composition of carbon-rich chondrites and the ∼20%wt carbon composition of Halley dust (Brownlee and Kissel, 1990), which confirm the high carbon abundance in comets.

The above conclusions depend on the amounts of material listed in Table 2. Among these numbers, the mass of dust in the hot plume is critical since it is the dominant contributor to the energy balance (41%). But it is also the least accurate, because of the assumptions on grain radius and density. The other mass estimates (and errors bars) should be robust because the required hypotheses to derive them are justified by the observations themselves (gas temperature for example) and/or because their contribution to the energy balance is negligible (velocity of the dust ejecta, for example). Our assumptions on grain radius (10 μm) and density (1000 kg/m^3) are justified in Section 3.1.5, and since these numbers give an energy balance in equilibrium, they seem particularly reasonable. But, from our observations alone, we cannot exclude the possibility that the typical grain radius is, say, 10 times larger (100 μm or more). In this case, the mass of dust would be 10 times larger, and the energy balance would no more be in equilibrium as the kinetic, melting and heating energies of the dust in the hot plume would be 3.5 times larger (∼70 GJ) than that of the impactor (19.7 GJ). This scenario, while it cannot be excluded, nevertheless

appears quite unlikely. Such a large amount of energy could be obtained in a short time by depressurization of a large gas pocket located at impact site. Assuming a gas pocket with a pressure of 10^3 Pa (upper limit, Section 4.2.3), the effective diameter of this pocket would have to be >0.5 km to deliver 70 GJ by depressurization, which seems unlikely for a nucleus with a mean radius of 3 km (Thomas et al., 2007). At this point, it is interesting to see that in the worst case where we are off by 5.9 GJ in our energy budget ($16.5 + 9.1 - 19.7$, see Table 2), a pocket of $\sim$0.2 km diameter would be sufficient to produce this extra energy, which is still large but more reasonable. Another possibility to add energy to the system is the crystallization of amorphous ice, which is an efficient exothermic process. The crystallization of 6.8×10^6 kg of amorphous water ice would liberate 600 GJ, so that even if only a small fraction of the water ice is in amorphous phase, it could add a lot energy to the system. However, as explained in Section 4.1, water ice is not expected to be in its amorphous phase in the first few meters of the surface.

Similarly, if we ignore the acceleration of dust ejecta grains by gas drag and assume that the average velocity of the dust ejecta is $\sim$160 m/s (Keller et al., 2007) and only results from the impact event, this would require 5 times the kinetic energy of the impactor ($\sim$95 GJ). Here, again depressurization of a large gas pocket could play a role, which is unlikely, but more importantly this would be in contradiction with the well-known acceleration effect of comet dust grains by gas drag, demonstrated experimentally by KOSI (Kochan et al., 1991). Overall, we strongly prefer the "simple" scenario presented in this paper and the numbers summarized in Table 2, which, we believe, are based on the most reasonable assumptions.

To conclude, the Deep Impact experiment has provided new insights into the composition of the upper layers of the comet. Our results emphasize the importance of laboratory impact experiments to understand the physical processes involved in such a large scale experiment. The Stardust-NExT mission in 2010, if it can observe the impacted area, will also greatly contribute to this understanding. Finally, it will be very interesting to compare and contrast our results with those expected from the Rosetta mission in 2014. In particular, the results from the Philae lander, which will perform a detailed analysis of the nucleus upper layers, will be crucial.

References

A'Hearn, M.F., and 32 colleagues, 2005. Deep impact: Excavating Comet Tempel 1. Science 310, 265–269.

Belyakov, G.V., Rodionov, V.N., Samosadnyi, V.P., 1978. Heating of porous material under impact compression. Combustion, Explosion and Shock Waves, vol. 13. Springer, New York.

Bockelée-Morvan, D., Crovisier, J., Mumma, M.J., Weaver, H.A., 2004. The composition of cometary volatiles. In: Festou, M.C., Keller, H.U., Weaver, H.A. (Eds.), Comet II. University of Arizona Press, Tucson, pp. 391–423.

Brownlee, D.E., Kissel, J., 1990. The composition of dust particles in the environment of Comet Halley. In: Mason, W. (Ed.), Comet Halley: Investigations, Results, Interpretations, Dust Nucleus Evolution, vol. 2. Ellis Horwood/Prentice-Hall, Chichester, England/Englewood Cliffs, NJ, pp. 89–98 (The Ellis Horwood Library of Space Science and Space Technology, Series in Astronomy).

Coradini, A., and 68 colleagues, 1998. VIRTIS: An imaging spectrometer for the Rosetta mission. Planet. Space Sci. 46 (9–10), 1291–1304.

Crovisier, J., 2006. New trends in cometary physics. Faraday Discuss. 133, 375–385.

Dominik, C., Tielens, A.G.G.M., 1997. The physics of dust coagulation and the structure of dust aggregates in space. Astrophys. J. 480, 647–673.

Ernst, C.E., Schultz, P.H., 2007. Evolution of the Deep Impact flash: Implications for the nucleus surface based on laboratory experiments. Icarus 190, 123–133.

Farnham, T.L., and 11 colleagues, 2007. Dust coma morphology in the Deep Impact images of Comet 9P/Tempel 1. Icarus 187, 26–40.

Feaga, L., A'Hearn, M.F., Sunshine, J.M., Groussin, O., Farnham, T.L., 2007. Tempel 1's H_2O and CO_2 inner coma asymmetries from Deep Impact observations. Icarus 190, 345–356.

Groussin, O., and the Deep Impact Team, 2005. Temperature map of the nucleus of Comet 9P/Tempel 1 from the Deep Impact mission. Bull. Am. Astron. Soc. 37, 703.

Groussin, O., A'Hearn, M.F., Li, J.-Y., Thomas, P.C., Sunshine, J.M., Lisse, C.M., Meech, K.J., Farnham, T.L., Feaga, L.M., Delamere, W.A., 2007. Surface temperature of the nucleus of Comet 9P/Tempel 1. Icarus 187, 16–25.

Hampton, D.L., Baer, J.W., Huisjen, M.A., Varner, C.C., Delamere, A., Wellnitz, D.D., A'Hearn, M.F., Klaasen, K.P., 2005. An overview of the instrument suite for the Deep Impact mission. Space Sci. Rev. 117, 43–93.

Holsapple, K.A., Housen, K.R., 2007. A crater and its ejecta: An interpretation of Deep Impact. Icarus 187, 345–356.

Jorda, L., Lamy, P., Faury, G., Keller, H.U., Hviid, S., Küppers, M., Koschny, D., Lecachauex, J., Gutiérrez, P., Lara, L.M., 2007. Properties of the dust cloud caused by the Deep Impact experiment. Icarus 187, 208–219.

Keller, H.U., and 38 colleagues, 2007. Observations of Comet 9P/Tempel 1 around the Deep Impact event by the OSIRIS camera onboard Rosetta. Icarus 187, 87–103.

Kochan, H., Markiewicz, W., Keller, H.U., 1991. KOSI – Gas drag derived from ice/dust particles trajectories. Geophys. Res. Lett. 18, 273–276.

Lisse, C.M., A'Hearn, M.F., Farnham, T.L., Groussin, O., Meech, K.J., Fink, U., Scleicher, D.G., 2005. The coma of Comet 9P/Tempel 1. Space Sci. Rev. 117, 161–192.

Lisse, C.M., and 16 colleagues, 2006. Spitzer spectral observations of the Deep Impact ejecta. Science 313, 635–640.

Meech, K.J., and 208 colleagues, 2005. Deep Impact: Observations from a worldwide Earth-based campaign. Science 310, 265–269.

Melosh, H.J., and the Deep Impact Team, 2006. Deep Impact: The first second. Lunar Planet. Sci. 37. Abstract 1165.

Mumma, M.J., and 13 colleagues, 2005. Parent volatiles in Comet 9P/Tempel 1: Before and after impact. Science 310, 270–274.

Patashnick, H., Rupprecht, G., 1977. The lifetime of ice particles in the Solar System. Icarus 30, 402–412.

Pierazzo, E., Melosh, H.J., 1999. Hydrocode modeling of Chicxulub as an oblique impact event. Earth Planet. Sci. 165, 163–176.

Prialnik, D., Benkhoff, J., Podolak, M., 2004. Modeling the structure and activity of comet nuclei. In: Festou, M.C., Keller, H.U., Weaver, H.A. (Eds.), Comet II. University of Arizona Press, Tucson, pp. 359–387.

Richardson, J.E., Melosh, H.J., Lisse, C.M., Carcich, B., 2007. A ballistics analysis of the Deep Impact ejecta plume: Determining Comet Tempel 1's gravity, mass, and density. Icarus 191, 176–209.

Schmitt, B., Espinasse, S., Grim, R.J.A., Greenberg, J.M., Klinger, J., 1989. Laboratory studies of cometary ice analogues. Phys. Mech. Comet. Mater. ESA-SP 302, 65–69.

Schultz, P.H., Ernst, C.M., Anderson, L.B., 2005. Expectations for crater size and photometric evolution from the Deep Impact collision. Space Sci. Rev. 117, 207–239.

Schultz, P.H., Eberhardy, C.A., Ernst, C.M., A'Hearn, M.F., Sunshine, J.M., Lisse, C.M., 2007. The Deep Impact oblique impact cratering experiment. Icarus 190, 295–333.

Sugita, S., and 22 colleagues, 2005. Subaru telescope observations of Deep Impact. Science 310, 274–278.

Sunshine, J.M., and 21 colleagues, 2006. Exposed water ice deposits on the surface of Comet Tempel 1. Science 311, 1453–1455.

Sunshine, J.M., Groussin, O., Schultz, P.H., A'Hearn, M.F., Feaga, L.M., Farnham, T.L., Klaasen, K.P., 2007. The distribution of water ice in the interior of Comet Tempel 1. Icarus 190, 284–294.

Thomas, P.C., and 16 colleagues, 2007. The shape, topography and geology of Comet Tempel 1 from Deep Impact observations. Icarus 187, 4–15.

Yeomans, D.K., Giorgini, J.D., Steven, R., 2005. The history and dynamics of Comet 9P/Tempel 1. Space Sci. Rev. 117, 123–135.